NUMERICAL SIMULATION OF AIRFOIL FLOWS WITH POROUS SURFACE SEGMENTS USING AN EDDY-VISCOSITY MODEL

A.C. Botelho e Souza[1], P. Kumar[1], M. Möβner[2], R. Radespiel[1]
[1] TU Braunschweig, Institute of Fluid Mechanics, Hermann-Blenk-Str. 37, 38108 Braunschweig
[2]Deutsches Zentrum für Luft- und Raumfahrt (DLR), Institute of Aerodynamics and Flow Technology – Technical Acoustics, Lilienthalplatz 7, 38108 Braunschweig

Abstract

This paper summarizes the results of the validation and calibration of a two-equation turbulence model for VRANS simulations of flow through porous media. The results herein are a continuation of a previous work during which a numerical model based on VRANS equations with a Reynolds stress turbulence model was developed for flow through porous media. The results obtained in this previous work were used as a reference for calculations performed with an eddy-viscosity model. Representative validation cases such as channels with porous bottom are used to verify the new two-equation model, followed by investigation of the flow over the DLR-F15 airfoil with a porous segment at the trailing-edge, where porosity effects on lift and turbulent kinetic energy are evaluated.

1. INTRODUCTION

Noise reduction is one of the main requirements for the modern aircraft design. Much of the research efforts have focused on minimizing airframe noise, particularly the one generated at the wing trailing-edge. The noise mechanisms related to sharp trailing-edges at high Reynolds number flows such as the ones used on civil aviation have been described in literature such as the work of Lighthill[1] and are known to be related to pressure variations and to turbulent flow and its fluctuations. However, the means to achieve a solid knowledge base regarding this noise source still poses challenges that must be overcome.

These challenges have been the focus of active research in recent years and can be considered as three-folded. Firstly, one must be able to accurately characterize such a noise source in order to analyze it in detail. Experimentally, this is not straight forward due to difficulties related to isolating the source in question from other overall source components and external sources and also due to scaling issues. On the other hand, numerical noise prediction is also related to known difficulties which can be found in papers such as the one of Wang et al [2], which illustrates how the inherent unsteadiness and multi-scale quality of high-Re turbulent flows require several modeling techniques and simplifications.

Secondly, the numerous attempts on attenuating trailing-edge noise have not led to a conclusive optimal approach, which takes into account the complexity of the subject. However, the high potential of permeable structures in this matter has been demonstrated by Herr [3]. By testing and analyzing the effect of various porous materials installed at the trailing-edge of an airfoil, the author concluded that this type of treatment might achieve up to 6 dB of broadband noise reduction.

Thirdly, noise attenuation by porous trailing-edges, although acoustically beneficial, contains a significant drawback. It is responsible for diminishing the airfoil aerodynamic performance, which must also be taken into account while evaluating the efficiency and suitability of a noise reduction strategy. Experimental difficulties on measuring the flow inside porous media contribute to justify the efforts on developing robust numerical tools. Nonetheless, as previously mentioned, this procedure is not straight forward since calculations on the pore level are very complex. Therefore, the usual approach is to apply a model to predict the behavior of the flow within/around it.

The vast majority of the research on turbulence modeling regarding porous media is highly driven by a specific application. Several approaches have been developed based on the k-ε turbulence model; as an example, with the purpose of applications on heat and mass transfer, Antohe and Lage [4] developed a model to predict turbulent behavior in complex geometries with porous materials from time-averaging the Navier-Stokes volume-averaged momentum equation, to which Darcy- and Forchheimer-terms were added to account respectively for viscous and form drag, and deriving from it the transport equations for turbulent kinetic energy and its dissipation rate. More recent models such as the one of Pedras and De Lemos [5] follow a different path by firstly employing the time-average operator followed by the volume-averaging procedure. The main differences on the resultant equations, as well as the relation between the two approaches, are described in [5].

Motivated by the need of modeling flow around and within porous media as required by aeronautical applications, Möβner [6] developed a model assuming compressible flow. Similarly to the work of Breugem [8], where DNS computations on partially porous channel cases were performed, he used VRANS equations and provided a special treatment to the nonporous-porous interface, which required extensive validation and calibration efforts documented in [6],[7]. The use of the transport equations in their compressible form, as well as a second-order closure model instead of an eddy-viscosity model, made the

approach more complete and broadened its range of applications in comparison to previous ones.

The model has shown good agreement with experimental measurements and DNS computations [[6],[8]]. The present work focuses on further enhancing the capabilities of the computational tool for aeronautical applications by providing validation and calibration of a two-equation turbulence model as a further option.

Representative porous channel cases were considered in order to verify the implemented porous terms on the relevant transport equations. Finally, more complex simulations of the flow over the DLR-F15 airfoil with porous trailing-edge were conducted in order to assess not only the performance of the model on reproducing measurements of turbulent quantities, but also the resultant loss of lift caused by the flow through the porous structure.

2. GOVERNING EQUATIONS

2.1. VRANS Momentum Equation

As mentioned in Section 1, the Navier-Stokes transport equations in their compressible form were volume-averaged and subsequently averaged in time. The detailed description of the procedure and derivation can be found in [6]. Due to the differences between the second-moment closure turbulence model definitions used by Möβner in [6] and the eddy-viscosity model considered herein, the compressible flow closure approximations for the energy conservation equation differ slightly and can be found in [9].

The equations describing mass and energy conservation are identical to the ones referring to non-porous flows and will therefore not be commented here. On the other hand, two additional terms are considered in the momentum conservation equation as follows:

$$(1)\ \frac{\partial \bar{\rho}\tilde{u}_i}{\partial t} + \frac{\partial \bar{\rho}\tilde{u}_i\tilde{u}_j}{\partial x_j} = -\frac{\partial \bar{\rho}\widetilde{u_i'u_j'}}{\partial x_j} - \frac{\partial \bar{p}}{\partial x_i} + \frac{\partial \bar{\tau}_{ij}}{\partial x_j} + P_v + P_f$$

$$P_v = -\frac{\phi\bar{\mu}}{\kappa}\tilde{u}_i;\ P_f = -\frac{\phi^2 c_F}{\sqrt{\kappa}}\bar{\rho}\widetilde{u_i|\mathbf{u}|}$$

in which ρ is density, t is time, u_i and x_i are, respectively, velocity components and Cartesian coordinates, p is pressure, τ_{ij} is the viscous-stress tensor and $\rho\widetilde{u_i'u_j'}$ is the Reynolds stress tensor. P_v represents the effect of viscous drag added to the flow by the porous medium. It depends on the permeability κ and on the porosity ϕ, which is defined as the ratio between the fluid volume V_f and the total volume V. This concept was initially developed by Darcy and later extended by Forchheimer, whose contribution, shown here as P_f, represents the effect of porous additional form drag. The Forchheimer coefficient c_F is a property of the porous medium, as well as the permeability κ.
The term P_f requires modeling and the approximation used by Möβner in [6] is used here in its reduced form so that only the first-order term of the Taylor expansion is considered, as follows:

$$(2)\ P_f = -\frac{\phi^2 c_F}{\sqrt{\kappa}}\rho\widetilde{u_i|\mathbf{u}|} \approx -\frac{\phi^2 c_F}{\sqrt{\kappa}}\rho\tilde{u}_i|\mathbf{u}|$$

A stress-dependent additional contribution is added to the Forchheimer term of equation (1) and will be described in the following subsection.

2.2. Turbulence Modeling

All numerical simulations conducted made use of a linear eddy-viscosity model, which is dependent on the Boussinesq approximation shown below to model the Reynolds stress tensor:

$$(3)\ -\bar{\rho}\widetilde{u_i'u_j'} = 2\mu_t\left(S_{ij} - \frac{1}{3}\frac{\partial \bar{u}_k}{\partial x_k}\delta_{ij}\right) - \frac{2}{3}\bar{\rho}k\delta_{ij}$$

$$S_{ij} = \frac{1}{2}\left(\frac{\partial u_i}{\partial x_j} + \frac{\partial u_j}{\partial x_i}\right)$$

in which S_{ij} is the strain-rate tensor, δ_{ij} is the Kronecker delta, k is the turbulent kinetic energy and μ_t is the eddy-viscosity; definitions can be found in [8] and the additional terms due to porous medium are briefly described in this section.

The choice of two-equation turbulence model was the Menter Shear Stress Transport (SST) model, which has been used successfully in predicting a wide range of aerodynamic flows with complex phenomena. In addition, it is broadly used in aeroacoustics analysis, which is relevant for the numerical tool in question and therefore its use would be of interest. The version developed in 1994 was used throughout this work and its definitions can be read in [10].

The porous terms added to the turbulent kinetic energy k transport equation are:

$$(4)\ P_v^{SST,k} = -2\frac{\phi\bar{\mu}}{\kappa}k;\ P_f^{SST,k} = -4\frac{\phi^2 c_F}{\sqrt{\kappa}}\bar{\rho}k|\mathbf{u}|$$

The respective terms added to the specific dissipation rate ω transport equation are:

$$(5)\ P_v^{SST,\omega} = -2\frac{\phi\bar{\mu}}{\kappa}\omega;\ P_f^{SST,\omega} = -2\frac{\phi^2 c_F}{\sqrt{\kappa}}\bar{\rho}\omega|\mathbf{u}|$$

It is also worth mentioning that from the modeling of the porous Forchheimer form drag contribution to the momentum equation in [6] stems a term dependent on the normal stresses; this term, therefore, must be added to equation (1) as a contribution of the turbulent kinetic energy and can be modeled as follows:

$$(6)\ P_f^k = -2\frac{\phi^2 c_F}{\sqrt{\kappa}}\bar{\rho}\frac{\tilde{u}_i}{|\mathbf{u}|}k$$

For the sake of simplicity, the definition of the scalar coefficients in all porous terms was based on the term-by-term derivation found in [6] for the Reynolds stress model. The results obtained with the use of these values showed good agreement with RSM simulations, which will be further discussed in the following sections.

2.3. Interface Treatment

The modified turbulence model equations discussed in Section 2 describe the flow inside porous regions. The terms added, however, do not consider the abrupt porosity

change at the nonporous-porous interface, which yields critical importance to this region. The approach used to model it was based on the works of Ochoa-Tapia and Whitaker [11] and De Lemos and Silva [12], according to which gradients of velocity, temperature and turbulent quantities are defined and empirically adjusted by jump coefficients while considering mass and energy conservation through the interface, as well as the velocity direction as constant. The jump relation imposed to velocity is:

$$(7)\quad \bar{\mu}_f \left.\frac{\partial \bar{u}_i}{\partial x_j}\right|_f - \bar{\mu}_p \left.\frac{\partial \bar{u}_i}{\partial x_j}\right|_p = (1-\phi)\Delta g_{ij}$$

$$(8)\quad \Delta g_{ij} = \beta \frac{\phi \bar{\mu}}{\sqrt{K}} \overline{u_{i,f}}$$

The indexes f and p define variables related to nonporous and porous regions, respectively. The configuration of equation (8) and its gradient are very similar to the approach followed by Ochoa-Tapia and Whitaker, whose jump coefficient β_{OTW} is related to the one used by Möβner according to:

$$(9)\quad \beta_{OTW} = (1-\phi)\beta$$

The correspondent relations valid for turbulent kinetic energy k (written in function of Reynolds stresses) and specific dissipation rate ω are, respectively:

$$(10)\quad \bar{\mu}_f \left.\frac{\partial \overline{u_i' u_j'}}{\partial x_j}\right|_f - \bar{\mu}_p \left.\frac{\partial \overline{u_i' u_j'}}{\partial x_j}\right|_p = (1-\phi)\Delta g_{SST,k} \qquad (i=j)$$

$$(11)\quad \Delta g_{SST,k} = \beta_t \phi \bar{\rho} \sqrt{K} \left(\tau_{ij} \frac{\partial u_i}{\partial x_j}\right)$$

$$(12)\quad \bar{\mu}_f \left.\frac{\partial \bar{\omega}}{\partial x_j}\right|_f - \bar{\mu}_p \left.\frac{\partial \bar{\omega}}{\partial x_j}\right|_p = (1-\phi)\Delta g_{SST,\omega}$$

$$(13)\quad \Delta g_{SST,\omega} = \beta_\omega \frac{\phi \bar{\mu}}{\sqrt{K}} \bar{\omega}$$

Unlike the previous gradient defined for velocity by equation (8), equation (11) differs significantly from the original approach proposed by De Lemos and Silva [12], in which the turbulent gradient depended directly on the turbulent quantity. In the present approach, the increase in turbulence is originated by the production term of the correspondent turbulent quantity equation, which can be seen between parenthesis in equations (11). The simulations conducted with these relations applied to the JHh-v2 Reynolds stress model[6] led to very good agreement to DNS results.

The coefficients β and β_t describe the intensity of the jump condition effect on the flow behavior at the interface. In this work, this effect is studied by varying these coefficients and comparing the results to the ones obtained with RSM. It is also worth mentioning that the jump condition for the length scale is also taken into account for the channel cases; nevertheless, there is a lack of validation data for this approach and therefore one must consider its further use with caution.

In [6] one can find an observation on the low decay of normal Reynolds stresses below the surface of a turbulent channel bounded by porous material. This was modeled by adding diffusion fluxes to their transport equations. This flux can be modeled according to the following equation:

$$(14)\quad \bar{\rho} D_{p,ij} = \frac{\partial}{\partial x_k}\left(c_{d,p} \frac{\bar{\rho}}{0.09} \frac{k}{\omega} \frac{\partial k}{\partial x_k}\right)$$

in which $c_{d,p}$ is a modeling constant which was also varied during validation phase.

3. RESULTS

The modifications described above were implemented into an adapted version of DLR's TAU code [13] and solved with the aid of hybrid unstructured grids. Numerical settings varied according to the test case simulated and will be described further in this section. The main objective of the study was to determine whether the approaches described in Section 2 are able to capture the physical phenomena occurring in low complexity flows such as channels with porous bottom, and in more complex flows such as an airfoil with a porous trailing-edge. Furthermore, the sensitivities to the modeling parameters β, β_t, β_ω and $c_{d,p}$ presented are evaluated. The porous medium in each case is characterized by its intrinsic properties, i.e., porosity ϕ, Forchheimer coefficient c_F and Darcy number, defined as the ratio between the permeability and the square of the case-dependent length scale. The values set for these properties for all test cases are shown in Table 1.

TAB 1. Porous properties of validation cases

	CUB Channel	**E80 Channel**	**DLR-F15 Airfoil**
ϕ	0.875	0.800	0.460
$Da = \frac{K}{H^2}$	$3.4 \cdot 10^{-4}$	$7.1 \cdot 10^{-6}$	$1.24 \cdot 10^{-10}$
c_F	0.026	0.19	0.10

3.1. CUB Channel Case

The setup of a channel with a porous bottom referred to as CUB case in [6] and [8] was reproduced in this work, where H is the height of the channel. The left and right sides of the grid are defined as symmetry planes, the inflow is periodic to the outflow and an artificial forcing term is responsible for driving the flow through the channel as a pressure gradient does in a non-periodic case. A scheme of the geometry is illustrated on Figure 1, where the porous region is shown as the gray zone.

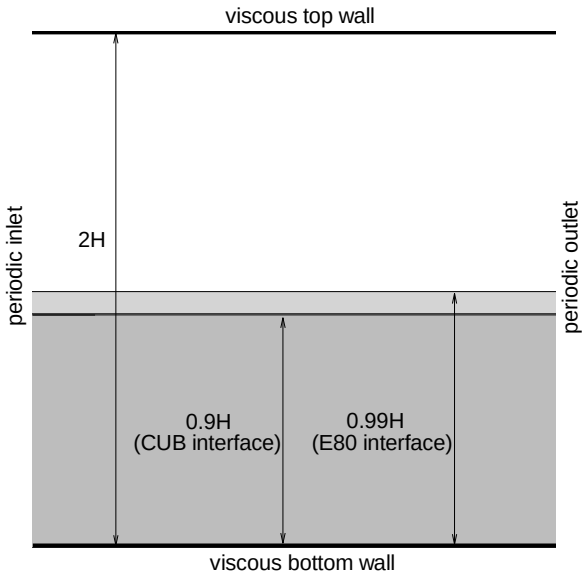

FIGURE 1: Sketch of channel geometry, with gray zone representing the porous bottom half

A grid convergence study was performed in [6] by varying the number of cells along the channel height and concluded that the solutions have very low sensitivity to this variation. Therefore, the present computation used the grid with intermediate coarsening, i.e., 360 cells along the height H. The upper wall and interface cell spacing are both equal to 2.10^{-4}H; if the friction Reynolds numbers calculated by Breugem as 394 at top wall and and 669 at interface are considered, a dimensionless wall spacing $\Delta y^+<1$ is obtained in both regions. The channel height is set as 1m and the interface is defined at 0.9H from the bottom viscous wall. The Reynolds number is adjusted to 5500 and is a function of the channel height and bulk velocity u_b = 27.5 m/s, defined as the mean velocity in the nonporous part. The Mach number is set to 0.15.

A second-order central discretization scheme was used to compute the convective fluxes of the mean flow equations. A first-order upwind Roe scheme was employed with the SST model in order to compute the convective turbulent fluxes. All channel computations were performed with a Backward Euler time-stepping scheme.

An initial assessment of the model's accuracy consisted on using the parameter setting suggested by Möβner in [6],[7] and shown in Table 2. This set was maintained for all RSM computations. Velocity profiles obtained are illustrated in Figure 2. Although the resulting match is already good in the porous region, it can still be improved by means of calibration, which was achieved by manually varying each of the jump parameters. The velocity and the turbulent kinetic energy profiles were established as key parameters to be compared, and due to the solutions' large sensitivity to the variations in question, the calibration method based on gradient observation was considered sufficiently precise.

TAB 2. Initial jump parameter setting

β	β_t	β_ω	$c_{d,p}$
-5	0.7	0	0.2

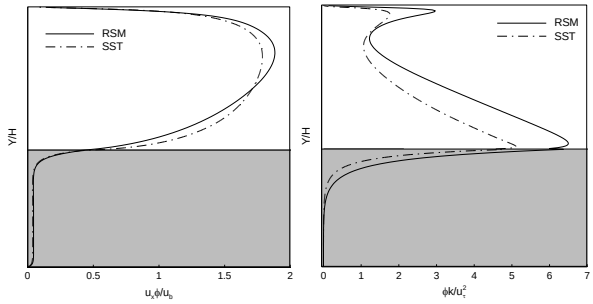

FIGURE 2: Velocity and turbulent kinetic energy profiles of CUB case with Menter SST and RSM turbulence models (β = -5, β_t = 0.7, β_ω = 0, $c_{d,p}$ = 0.2)

3.1.1. Effect of β variation

The calibration procedure consisted of varying one parameter at a time, starting by the jump coefficient β. As previously mentioned, it induces a jump on the velocity at the interface. Figure 3 illustrates this effect on the velocity profile and it can be seen that more negative values of β lead to smaller velocities at the interface, i.e., intensifies the jump. Within the porous region, all curves present a satisfactory match with RSM; the best match with RSM at interface was obtained for β = -7.3. It is worth mentioning that positive values of this parameter resulted in strong instabilities and crashed computations, which might be explained by the rapid increase of the Reynolds stresses under this condition, which highlights the need of evaluating the effect of β_t. A slight effect of β variation could also be observed on the turbulent kinetic energy profiles, which emphasizes the strong coupling of all transport equations considered herein.

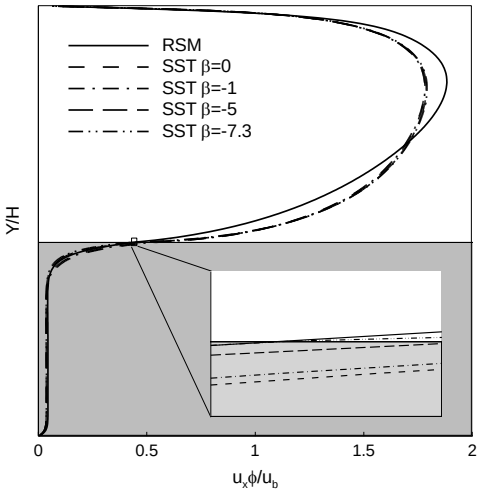

FIGURE 3: Velocity profiles of CUB case with variations in β (β_t = 0.7, β_ω = 0, $c_{d,p}$ = 0.2)

3.1.2. Effect of β_t variation

Despite of this effect of β on the turbulence quantity evaluated, the coefficient which is mainly responsible for controlling the behavior of this variable at the interface is β_t. Figure 4 shows a strong under-prediction of turbulence at interface of Menter SST with respect to RSM; a large difference between the values of turbulent kinetic energy obtained with the eddy-viscosity model and with RSM is expected, given that the latter is able to compute the Reynolds stresses more accurately with separate

transport equations for each of them, while the Menter SST model is only able to predict them as isotropic. To compensate this drawback and increase the agreement with the RSM curve, β_t was set to 2.0, a considerably higher value than the initial one. Higher values of β_t led to higher values of k at interface and also to slightly higher values of k inside the porous region. No significant changes were detected at the velocity profile while varying the turbulent jump coefficient.

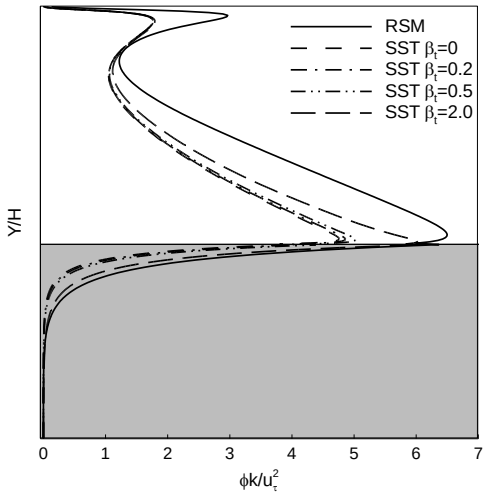

FIGURE 4: Turbulent kinetic energy profiles of CUB case with variations in β_t (β = -7.3, β_ω = 0, $c_{d,p}$ = 0.2)

3.1.3. Effect of $c_{d,p}$ variation

With β and β_t defined, the additional diffusion coefficient $c_{d,p}$ was varied as shown in Figure 5. The results corroborate the role of this additional term, i.e., the increase in curvature inside the porous region for higher values of $c_{d,p}$ indicates higher diffusion of the normal Reynolds stresses. In this case, $c_{d,p}$ = 0.2 was maintained for this coefficient.

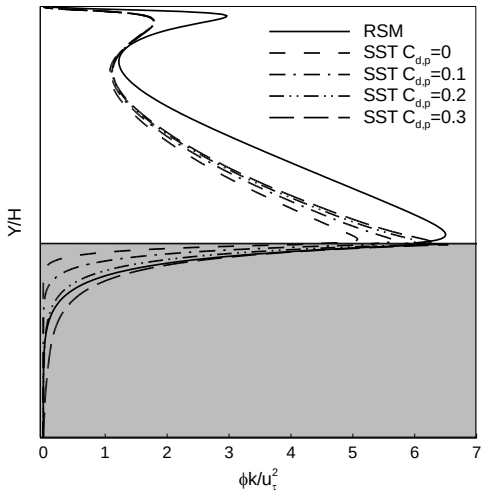

FIGURE 5: Turbulent kinetic energy profiles of CUB case with variations in $c_{d,p}$ (β = -7.3, β_t = 2.0, β_ω = 0)

3.1.4. Effect of β_ω variation

The last parameter to be varied was β_ω, which is responsible for the intensity of length scale jump at the nonporous-porous interface. In Figure 6 it can be seen that the sensitivity of the turbulent kinetic energy to this variation is very small. In addition, no significant change was observed on velocity profiles. Therefore, given the lack of validation for the jump condition equation considered for the length scale, it was decided to maintain this parameter as zero.

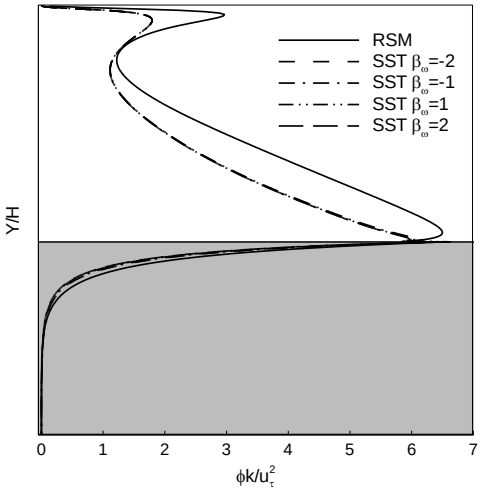

FIGURE 6: Turbulent kinetic energy profiles of CUB case with variations in β_ω (β = -7.3, β_t = 2.0, $c_{d,p}$ = 0.2)

3.2. E80 Channel Case

While the previous case validated the model for high permeabilities, the channel case referred to as E80, whose porous properties are described in Table 1, represents a test on the accuracy level for porous media with low permeabilities. The mesh has 300 cells along the height, which is considered suitable based on the grid convergence study performed for the previous case. Interface is set at 0.99H from the bottom viscous wall as illustrated in Figure 1. The correspondent upper wall and interface cell spacing are 5.10^{-4}H and 1.10^{-5}H and the respective friction Reynolds numbers are 354 and 398, resulting on Δy^+<1 in both regions. Reynolds and Mach numbers are maintained equal to CUB channel. In this case, since the effects of the jump coefficients were already analyzed, only the result obtained with the final set of parameters is shown in Figure 7:

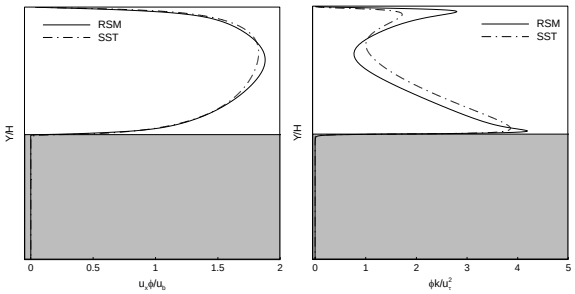

FIGURE 7: Velocity and turbulent kinetic energy profiles of E80 case with Menter SST and RSM turbulence models (β=0, β_t=0, β_ω=0, $c_{d,p}$=0)

Difficulties regarding convergence were observed in this case. Computations required the use of a previously converged RSM solution as starting computation point. The best match with RSM results was obtained when jump coefficients were set to zero. Good agreement with RSM results was predicted for velocity and turbulence kinetic

energy as illustrated in Figure 7. Due to the reduced permeability, velocities inside the porous region are even smaller than the ones observed for CUB case. The same behavior is detected for turbulence.

The final set of parameters for both channel cases are shown in Table 3:

TAB 3. Final jump parameter setting

	β	β_t	β_ω	$c_{d,p}$
CUB Channel	-7.3	2.0	0	0.2
E80 Channel	0	0	0	0

4. DLR-F15 AIRFOIL WITH POROUS TRAILING-EDGE

4.1. Numerical Settings and Flow Conditions

The DLR-F15 airfoil with porous trailing edge was the most relevant case of this study because it provided interesting insights about the performance of the model for an aeronautical application. Unlike the channel cases, the numerical simulations of porous segments in airfoil computations enabled the investigation of the effects on not only velocity and turbulent kinetic energy profiles, but also on aerodynamic characteristics such as the lift coefficient.

The same DLR-F15 airfoil geometry and 2D-grid setup used in [6] and illustrated in Figure 8, with around 40000 points used in [6], was reproduced here eliminating the need of further grid convergence investigations. The porous trailing-edge segment consists of 10% of the airfoils' chord length of 0.3m. Due to promising noise reduction results shown in [3], the porous properties of the porous aluminum material referred to as PA 80-110 was considered in this work and are shown in Table 1. In addition to porous simulations, clean airfoil computations were also performed for comparison purposes. Flow conditions are defined by a Reynolds number of 1.10^6, Mach number of 0.15 and transition at the lower and upper wall are set at 10 % and 5% of the chord length, respectively.

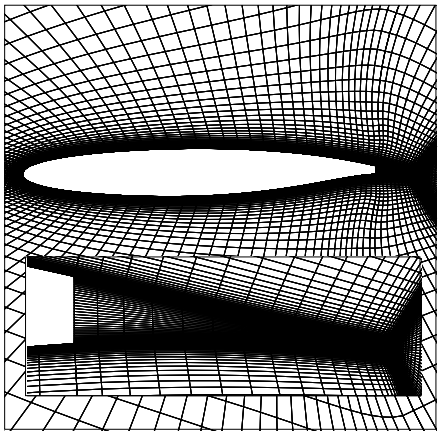

FIGURE 8: Grid of DLR-F15 airfoil with porous trailing-edge

The discretization schemes of mean flow and turbulent fluxes were maintained as in the channel cases, whereas the relaxation solver was switched to explicit Runge-Kutta. Convergence was assessed based on the behavior of the aerodynamic coefficients and was considered as reached when the difference in lift coefficient value between 1000 iterations was of the order of 10^{-5}. Figure 9 exemplifies the development of the lift and drag coefficients during these iterations for α=0º:

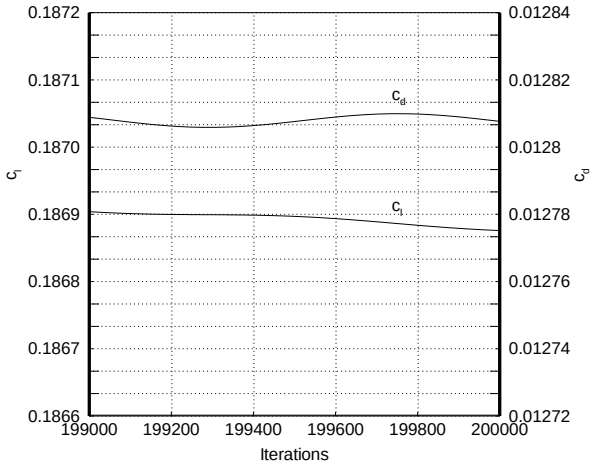

FIGURE 9: Evolution of lift and drag coefficients during last 1000 iterations for Menter SST model at α = 0º

It is worth mentioning that the normalized density residuals observed for the specific dissipation rate ω was higher than the residuals of other parameters; since similar behavior was observed on clean (i.e., without porous surfaces) airfoil computations, and taking into account the sufficient stability of the lift and drag coefficients on all computations, the results are considered to be reliable and suitable for further analysis. In addition, due to the lack of a proper reference for validation, jump coefficients were set to zero in all airfoil simulations.

4.2. Flow Field Behavior

Computations were performed for a range of angle of attack of -2º to 8º. By analyzing velocity contours of the porous airfoil in Figures 10 and 11, the main physical phenomena caused by the presence of porous medium is demonstrated; due to the pressure gradient, the flow crosses the trailing-edge from the pressure to the suction side, changing the camber of the streamlines at the upper surface. The resultant pressure difference between suction and pressure side decreases leading to lift loss.

While no significant difference is observed between the flow field behaviors obtained with both models for the clean airfoil, it can be seen that a slightly higher streamline decambering by boundary layer displacement is predicted by Menter SST at low and high angles of attack for the porous trailing-edge.

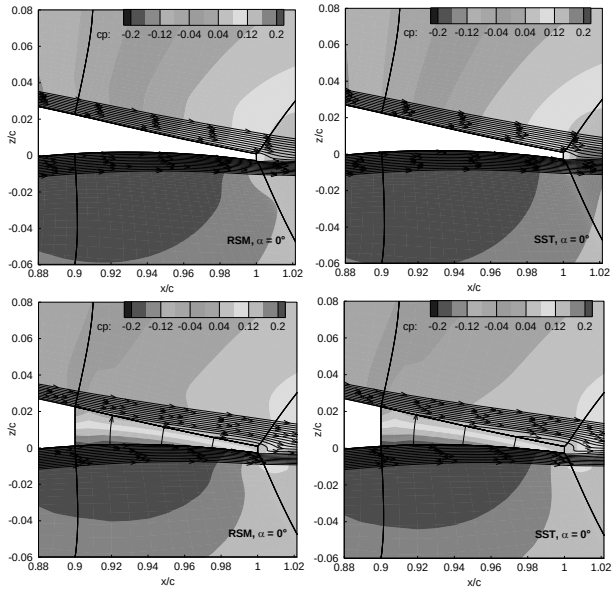

FIGURE 10: Pressure contour plots for clean and porous airfoil at α = 0º

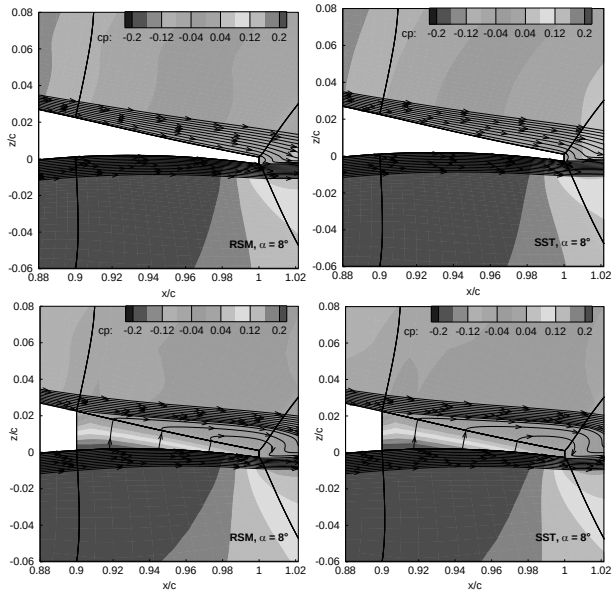

FIGURE 11: Pressure contour plots for clean and porous airfoil at α = 8º

The effect of the porous damping terms that model the flow inside the porous region becomes apparent on the turbulent kinetic energy contour plots of Figures 12 and 13 as a great reduction is observed in this region, as well as slightly above it. On the other hand, the increase in velocity gradients downstream from the trailing-edge, observed on the previous plots, leads to an augmentation of turbulence production in this area.

The differences between the Menter SST and RSM in the predicted turbulence distribution is apparent from the clean airfoil computations. These differences are larger for the porous trailing-edge case and increase with angle of attack, mainly downstream from the trailing-edge; a more detailed analysis will be shown below.

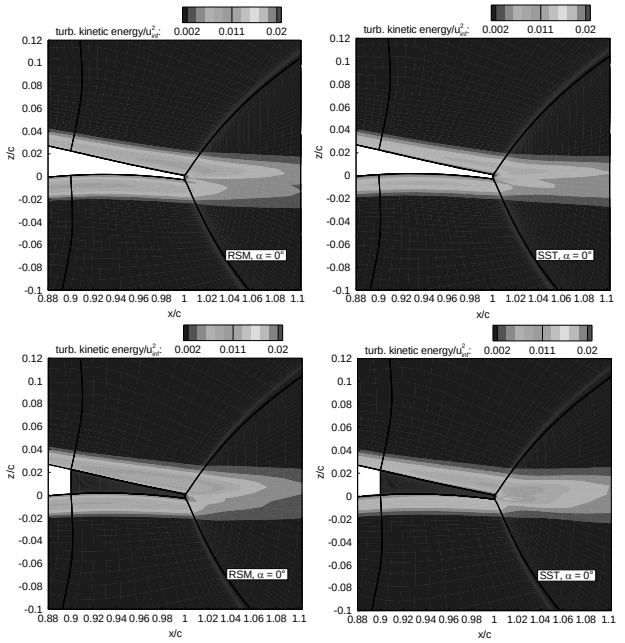

FIGURE 12: Turbulent kinetic energy contour plots for clean and porous airfoil at α = 0º

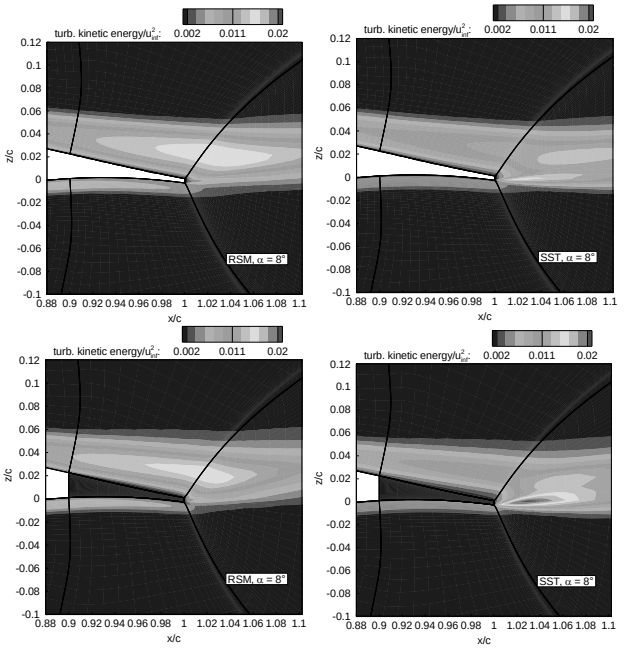

FIGURE 13: Turbulent kinetic energy contour plots for clean and porous airfoil at α = 8º

4.3. Effect of Porous Surface on Lift

As previously mentioned in this paper, a loss of lift is expected due to the presence of porous medium. In Figure 14 are plotted not only numerical results but also experimental ones, obtained by Möβner and reported in [6]. The experiment represented a two-dimensional wing with cross-section defined as the DLR-F15 airfoil, span of 1.3m and chord of 0.3m. The porous surface had 0.03m of chord and 0.3m of span. The same flow conditions described here were applied and PIV as well as pressure measurements were performed.

The gap in lift between experimental and numerical results is higher for the clean case than for the porous case. The eddy-viscosity model predicts higher lift in both cases. The highest loss of lift occurs at $\alpha = 4^o$ for both turbulence models; the maximum difference in c_l between clean and porous simulations at this angle of attack is $\Delta c_l = 0.085$ for RSM and $\Delta c_l = 0.070$ for Menter SST. In general, both models show good agreement with the experimental values for the porous airfoil.

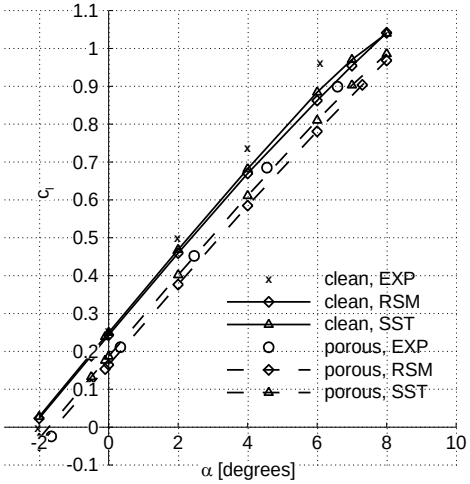

FIGURE 14: Comparison of lift curves between numerical and experimental results

4.4. Boundary Layer Profiles

Velocity and turbulence profiles of the boundary layer region were plotted at a point located at the suction side above the trailing-edge (x/c = 0.940) and at a point downstream (x/c = 1.050). The comparison was made using the same lift coefficient predicted by each of the models and measured by the experiment. These values are slightly different depending on the case; however, the angle of attack respective to each lift coefficient did not differ greatly among the turbulence models, as illustrated in Table 4.

TAB 4. Lift coefficients and respective angles of attack for the comparison of boundary layer profiles

	Clean Airfoil		Porous Airfoil	
c_l	0.193	0.953	0.157	0.898
EXP	-0.50º	6.0º	-0.50º	6.0º
RSM	-0.50º	7.0º	-0.10º	7.3º
SST	-0.51º	6.8º	-0.27º	6.9º

All values are normalized with the freestream velocity u_{inf}. In the case of clean airfoil, Figure 15 illustrates that the agreement of the velocity profiles among all curves is quite good at the point more upstream for low c_l. If results are compared at the same conditions for porous case in Figure 16, it can be seen that both turbulence models predict a boundary layer with less momentum, and this effect is slightly larger than in experiment. Interestingly, wake velocities are under-predicted by SST for all conditions considered.

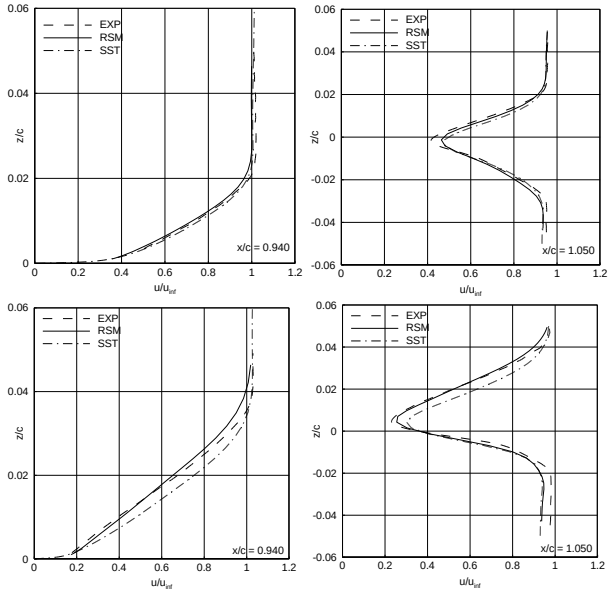

FIGURE 15: Comparison of boundary layer velocity profiles for clean airfoil at $c_l = 0.193$ (upper plots) and $c_l = 0.953$ (lower plots)

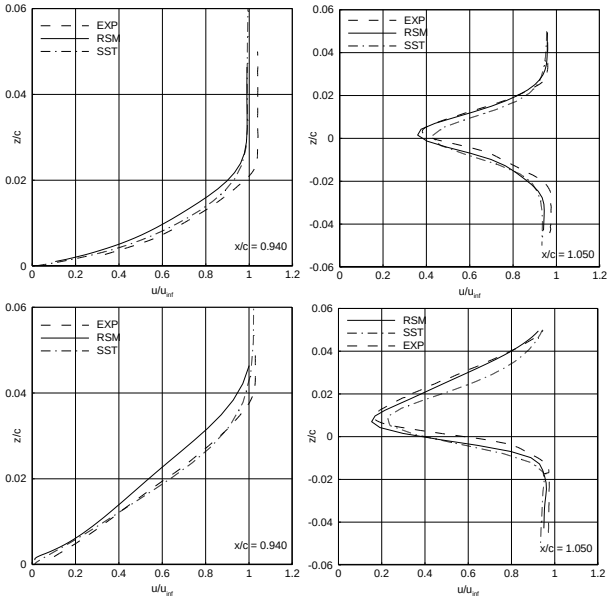

FIGURE 16: Comparison of boundary layer velocity profiles for porous airfoil at $c_l = 0.157$ (upper plots) and $c_l = 0.898$ (lower plots)

The choice of turbulence quantity for comparison originated from the experiment, as only normal stresses in x- and z-directions were measured. It is apparent that both models predicted higher turbulence values for the porous case in comparison to their respective clean airfoil computations, which corroborates the conclusions resultant from the evaluation of the field plots and is in agreement with what was measured experimentally. From Figures 17 and 18, a general trend appears in the results at the position above the trailing-edge. In both cases, Menter SST under-predicts turbulence while RSM over-predicts it with respect to values detected in the experiment. This discrepancy might be explained by the intrisic characteristic of the eddy-viscosity model of not considering the anisotropy of the stresses leading to a loss of accuracy especially near walls. In addition, both models

present poor agreement with experiment at the wake for low and high c_l values.

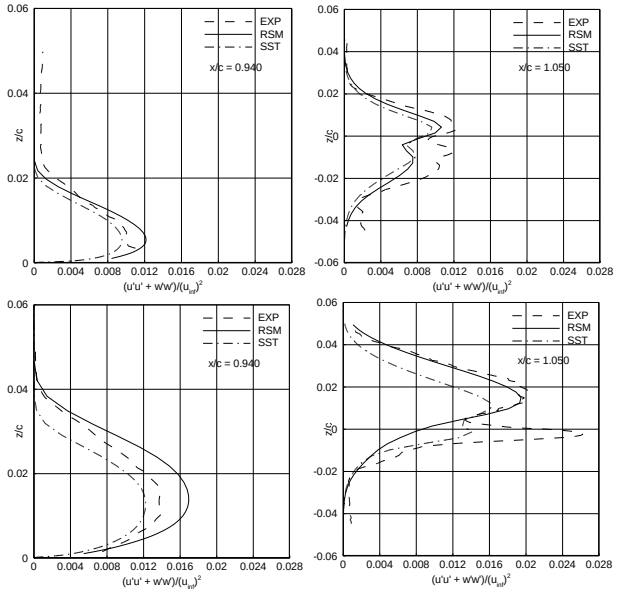

FIGURE 17: Comparison of boundary layer turbulence profiles for clean airfoil at c_l = 0.193 (upper plots) and c_l = 0.953 (lower plots)

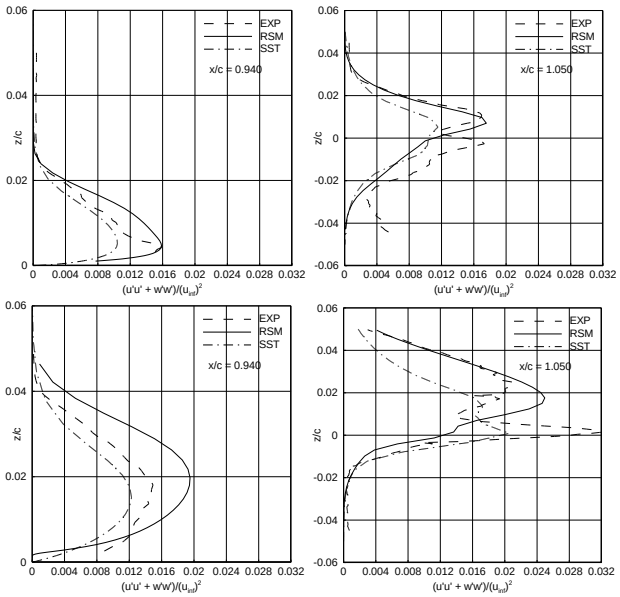

FIGURE 18: Comparison of boundary layer turbulence profiles for porous airfoil at c_l = 0.157 (upper plots) and c_l = 0.898 (lower plots)

5. CONCLUSION

Results of numerical simulations using an extended Menter SST turbulence model for channels with a porous bottom and of the DLR-F15 airfoil with porous trailing-edge have been presented. The channel flow was used to calibrate model constants. The velocity and turbulent kinetic energy profiles obtained with this calibrated constants reflect the best match with previously obtained RSM results.

The Menter SST turbulence model was subsequently applied to a more complex case. The DLR-F15 airfoil was considered; velocity and turbulence behaviors could be evaluated and compared to previously provided RSM and experimental results. The main physical mechanisms resultant from the presence of a porous medium are reproduced by the eddy-viscosity model. A quantitative analysis of the effect of the porous surface on lift was performed and, as expected, the Menter SST model predicts a loss of lift in accordance with what was detected by RSM and measured by experiment. It was found that Menter SST model generally under-predicts turbulence above the trailing-edge of the airfoil. The analysis of the airfoil near wake revealed that both Menter SST and RSM models achieve less accurate turbulent predictions in the wake.

The present results highlight the potentials and limits of modeling the flow inside and around porous media with a turbulence eddy-viscosity model. It is worth noting that the additional terms to the transport equations described herein were based on the ones developed for a Reynolds stress model; since no term-by-term derivation was performed, modeling inaccuracies might have influenced the final results.

ACKNOWLEDGEMENTS

This work was conducted within the frame of the Collaborative Research Center SFB 880 - Fundamentals of High-Lift for Future Civil Aircraft [14], which is funded by the Deutsche Forschungsgemeinschaft.

REFERENCES

[1] Lighthill, M.J., *On Sound Generated Aerodynamically -I. General Theory*, Proc. R. Soc. London Ser. A 211(1107), pp.564–87 (1952)

[2] Wang, M., Freund, J.B., Lele, S.K., *Computational Prediction of Flow-Generated Sound*, Annu. Rev. Fluid Mech., Vol.38, pp.483–512 (2006)

[3] Herr, M. et al, *Specification of Porous Materials for Low-Noise Trailing-Edge Applications*, 20th AIAA/CEAS Aeroacoustics Conference, AIAA-2014-3041, Atlanta, Georgia, June (2014)

[4] Antohe, B.V., Lage, J.L., *A General Two-Equation Macroscopic Turbulence Model for Incompressible Flow in Porous Media*, Int. J. Heat Mass Transfer, Vol. 40, No. 13, pp.3013-3024 (1997)

[5] Pedras, M.H.J., De Lemos, M.J.S., *Macroscopic Turbulence Modeling for Incompressible Flow Through Undeformable Porous Media*, Int. J. Heat Mass Transfer, Vol. 44, pp.1081-1093 (2001)

[6] Möβner, M., *Volume-Averaged RANS-Simulations of Turbulent Flow over Porous Media*, Ph.D. Thesis,NFL Forschungs-bericht 2016-01 ISBN 978-3-928628-79-2 (2016)

[7] Möβner, M., Radespiel, R., *Modelling of Turbulent Flow over Porous Media Using a Volume Averaging Approach and a Reynolds Stress Model*, Computers \& Fluids, Vol. 108, pp.25–42 (2015)

[8] Breugem, W.P., *The Influence of Wall Permeability on Laminar and Turbulent Flows*, Ph.D. Thesis, Technische Universiteit Delft (2005)

[9] Wilcox, D.C., *Turbulence Modeling for CFD*, pp.249-256, 3rd. ed., DCW Industries (2006)

[10] Menter, F.R., *Two-Equation Eddy-Viscosity Turbulence Models for Engineering Applications*, AIAA Journal, Vol. 32, No. 8, pp.1598-1605 (1994)

[11] Ochoa-Tapia, J.A., Whitaker, S., *Momentum Transfer at the Boundary between a Porous Medium and a Homogeneous Fluid - I. Theoretical Development*, Int. J. Heat Mass Transfer, Vol. 38, pp.2645-2646 (1995)

[12] De Lemos, M.J.S., Silva, R.A., *Turbulent Flow over a Layer of Highly Permeable Medium Simulated with a Diffusion-Jump Model for the Interface*, Int. J. Heat Mass Transfer, Vol. 49, pp. 546-556 (2006)

[13] Schwamborn, D., Gardner, A., von Geyr, H., Krumbein, A., Lüdeke, H., Stürmer, A., *Development of the TAU-Code for Aerospace Applications*, Proceedings of the 50th NAL International Conference on Aerospace Science and Technology, Bangalore, India (2008)

[14] Radespiel, R., Heinze, W., *SFB880 - Fundamentals of High-Lift for Future Commercial Aircraft*, CEAS Aeronautical Journal, Vol. 5, No. 3, pp. 239-251 (2014)